PHASE TRANSFORMATIONS AND ELECTROTHERMAL EFFECTS IN EDM-MACHINED STEEL: SURFACE TOPOGRAPHY, CRATER MORPHOLOGY, AND DEBRIS EVOLUTION

I. MESSAOUDI[1], B. BEN FRAJ[2], H. HENTATI[1,3], M. TRABELSI[4], T. KAMOUN[4], W. MESLAMENI[4], M. HADDAR[1]

[1] LA2MP Laboratory, University of Sfax, Tunisia
E-mails: messaoudiikram119@gmail.com; mohamed.haddar2016@gmail.com
[2] Nanomaterials and Systems for Renewable Energy Laboratory, Research and Technology Center of Energy, Technopole Borj Cedria, Hammam Lif, Tunisia
E-mail: boutheina.benfraj2024@gmail.com
[3] ESSTHS, University of Sousse, Tunisia
E-mail: hamdi.hentati@yahoo.fr
[4] Higher Institute of Technological Studies of Sfax, Tunisia
E-mails: mounir.trabelsi@emp.tn; taoufikkamoun@yahoo.fr; meslameni.walid@gmail.com

Received March 20, 2025

Abstract. This study investigates the physical and microstructural properties of EDM-machined steel under varying electrical discharge machining (EDM) conditions. An experimental approach is adopted to evaluate the influence of pulse time (*Ton*), rest time (*Toff*), and discharge current (*I*) on material removal rate (*MRR*) and surface roughness (*Ra*). The effect of discharge energy on crater formation, debris evolution, and microstructural transformations is analyzed. Surface integrity is assessed through microscopic roughness analysis, crater morphology measurements, and X-ray diffraction (XRD) to reveal phase transformations induced by electrothermal effects.

Key words: Physical properties, microstructural analysis, EDM process.

DOI: https://doi.org/10.59277/RomJPhys.2025.70.912

1. INTRODUCTION

Physical properties of fabricated components, as well as the performance of related manufacturing processes, are widely studied, highlighting their crucial role in the engineering industry. This includes forming processes, which involve shaping materials through plastic deformation, enabling the production of complex geometries with enhanced mechanical properties [1, 2]. Welding techniques involve the application of heat to join materials, leading to the formation of a heat-affected zone (HAZ), which effects thermo-mechanical properties and causes complex microstructural transformations [3]. Additive manufacturing, has revolutionized prototyping and small-scale production by allowing layer-by-layer fabrication of complex structures with minimal material waste [4, 5]. Cutting processes work by fracturing the workpiece, with a primary focus on analyzing ductile damage mechanisms and enhancing cutting efficiency [6, 7], especially in machining operations. To enhance the understanding and prediction of the physical and damage-related properties of machined components, significant research efforts have been directed toward advanced material characterization and mechanical property improvement. These efforts are mainly categorized into two approaches: numerical modeling, which enables predictive analysis and process optimization, and experimental studies, which provide valuable insights into real-world machining behavior [8–9]. In machining, two categories of processes exist, which are conventional and non-conventional methods. In fact, the conventional machining includes traditional techniques such as turning and milling, which rely on direct contact between the tool and the material. Non-conventional machining, in contrast, employs alternative energy sources, such as electrical, thermal, or chemical energy, to remove material without direct mechanical contact [10–12].

Our focus is on the electrical discharge machining (EDM) process, which is extensively used for machining rigid and hard-to-cut materials. EDM is particularly valued for its ability to machine materials with varying hardness levels while minimizing tool wear, making it as a highly efficient manufacturing technology for precisely processing all electrically conductive materials [13]. Nitu *et al.* [14] fabricated precise slits by EDM process for fracture mechanics testing in pin load tension. A cycling pre-crack in the slit is then introduced to ensure accurate fracture mechanics evaluation. The slit dimensions are measured using an optical microscope, and metallographic analyses are conducted. Experimental investigations further reveal that electrode wear is highly dependent on process parameters, affecting the accuracy and surface quality of the machined parts [15, 16]. Marrocco *et al.* [17] conducted an experimental study to evaluate the influence of various EDM process parameters on the material removal rate and tool wear rate. Ramachandra [18] used the Response Surface Methodology (RSM) technique to optimize the EDM machining parameters for AISI 316 stainless steel. He developed a robust model that determined the optimal settings for achieving the EDM machining performance.

The main objective of our study is to predict the physical and microstructural properties of parts obtained through EDM under different machining conditions. An experimental investigation is conducted to analyze the effect of three key EDM machining parameters, which are the pulse time (*Ton*), the rest time (*Toff*), and the discharge current (*I*) on the material removal rate (*MRR*) and the surface roughness (*Ra*) of the machined parts.

2. METHODS AND MATERIALS

2.1. PHYSICAL PROPERTIES OF MATERIAL PARTS

Non-alloy steel C45 was selected as the workpiece material, while a copper electrode was used for EDM machining. Table 1 presents the chemical properties of the workpiece.

Table 1

Mechanical and chemical composition of C45

Tensile strength (N/mm^2)	Yield stress (N/mm^2)	Hardness (HB)	Density (g/cm^3)
560 – 620	275 – 340	170	7.85
C(%)	S(%); P(%)	Mn(%)	Si(%)
0.50 – 0.52	≤ 0.035	0.50 – 0.80	0.40 max

Copper is widely used as an electrode in EDM thanks to its high electrical and thermal conductivity, enabling efficient energy transfer and rapid heat dissipation. It also offers good machinability and wear resistance, ensuring greater precision for various applications. The physical properties of the electrode material are shown in Table 2.

Table 2

Physical properties of the electrode material

Electrical resistivity (10 – 8 Ωm)	Temp. melting (°C)	Hardness (HB)	Density (g/cm^3)
1.72	1083	70	8.89

The dielectric fluid used in the experiments is mineral oil, chosen for its essential properties suited to this machining process.

2.2. EXPERIMENTAL SET UP OF EDM PROCESS

To ensure consistency, the machining depth is maintained constant across all tests, while the machining time is recorded in real time using a digital stopwatch with an accuracy of ±1 ms.

In addition, the masses of both the workpieces and electrodes are measured before and after machining using a digital scale with a precision of ± 0.01 g. This study focuses on investigating the effect of three EDM machining parameters, which are pulse time (*Ton*), rest time (*Toff*), and discharge current (*I*) on the material removal rate (*MRR*) and the surface roughness (*Ra*) of workpiece.

- *Ton* is the length of time during which the voltage is applied.
- *Toff* is the period during which discharges are not allowed, providing time for electrode cooling, debris removal, and renewal of the dielectric fluid.
- *I* is the magnitude of the current flowing through the plasma.
- *MRR* refers to how quickly material is eroded from the workpiece due to electrical discharges. In the present study, *MRR* is measured by weighing the workpiece before and after machining, then using the weight difference to calculate how much material has been removed.

- *Ra* is the surface roughness, the key indicator of a workpiece surface quality after machining. It is typically measured in micrometers (µm) and its value is commonly determined through a topographical analysis.

The EDM parameters are selected in three levels for each parameter as shown in Table 3. The selected plan is the full factorial 33 = 27 tests.

Table 3

Input parameters levels

Parameters	Level 1	Level 2	Level 3
I (A)	8	24	64
Ton (µs)	8	100	1600
Toff (µs)	4	25	200

2.3. MICROSTRUCTURAL AND TOPOGRAPHICAL METHODS

Surface quality of the machined samples was determined by using digital roughness tester and profilometer. Surface roughness measurements are conducted in the central region of the machined surfaces to minimize potential effects from thermal gradients or debris accumulation near the surface edges. The measurements by the profilometer are taken over a (1×1 mm^2) section with a fixed sampling interval of 20 µm. Multiple scans are made at different locations on each surface. The surface finish of the machined samples was characterized by the arithmetic average roughness (*Ra*).

The discharge crater size is measured using an optical microscope with 50× and 25× objective lenses. For phase structure analysis, X-ray diffraction (XRD) is conducted using a D8 Advance X-ray diffractometer, with a 2θ range from 40° to 85° and a scanning step size of 0.02°. Copper Kα radiation was used for the XRD measurements.

3. RESULTS AND DISCUSSION

3.1. MEASURED MATERIAL REMOVAL RATE AND SURFACE ROUGHNESS

Based on the measured values of *MRR* and *Ra*, the effects of the machining parameters on these two factors will be analyzed. The average value of an outcome is determined using Equation (1):

$$Y = \frac{\sum_{i=1}^{N} X}{N} \tag{1}$$

where *Y* is the mean outcome value, *X* represents the individual response values for the outcome from the EDM tests, and *N* is the total number of experimental measurements at a specific parameter level.

Figure 1 illustrates the correlation between the applied current *I* and the outcomes, which are *MRR* and *Ra*. As the current *I* rises from 8 A to 64 A, *MRR* demonstrates a pronounced linear increase. This phenomenon is attributed to the heightened energy density at the spark interface with increasing current, thereby growing the erosion process on the workpiece surface. Consequently, a higher *MRR* indicates increased material removal per discharge. Moreover, this elevated energy input also influences surface quality.

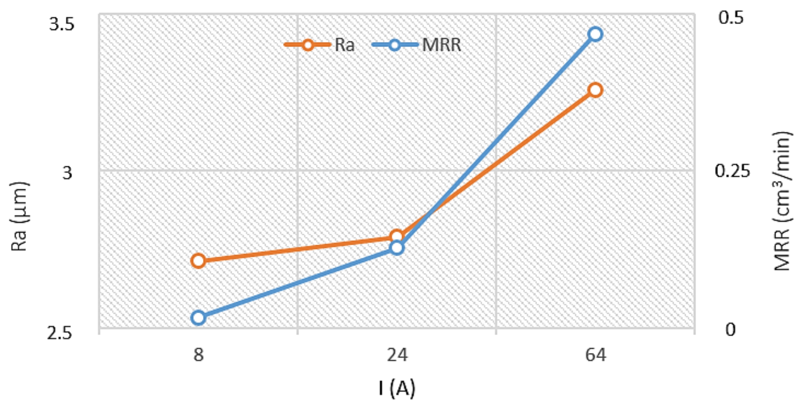

Fig. 1 – Effect of *I* on *MRR* and *Ra*.

Higher current intensities result in more aggressive material removal, leading to deeper surface features and, consequently, higher *Ra*. This effect was observed on the machined surface of the Ti-6Al-4V alloy using a molybdenum electrode, where an increase in *I* caused more pronounced material ejection, resulting in a rougher surface [19]. The dependence of *MRR* and *Ra* on *Ton* is showed in Fig. 2. As *Ton* increases from 8 µs to 1600 µs, both *MRR* and *Ra* show a significant rise, approximately from 0.05 to 0.30 cm^3/min and 2.4 µm to 3.2 µm, respectively. The increase is particularly pronounced at lower *Ton* values (8 µs to 100 µs) with a tendency to plateau at higher *Ton* values, indicating a saturation effect in material removal efficiency. The initial sharp increase in *MRR* and *Ra* with increasing *Ton* is attributed to the higher energy input per discharge, which enhances material melting and vaporization. However, as *Ton* continues to rise, material removal efficiency declines due to factors such as plasma channel expansion and increased debris accumulation, which can obstruct the erosion process [20, 21].

In the same context, the dependence of *MRR* and *Ra* on *Toff* is presented in Fig. 3. The curves indicate an inverse correlation between *Toff* and *MRR* as *Toff* increases from 25 µs to 200 µs.

This reduction in *MRR*, approximately 30%, follows a sharp increase of 243% when *Toff* rises from 4 µs to 25 µs. The decrease in *MRR* can be attributed to longer *Toff*, which increases the interval between successive discharges, reduces the frequency of electrical pulses, and consequently lowers the energy delivered to the material [22]. In contrast, *Toff* exhibits a direct correlation with *Ra*, as higher *Toff* values lead to increased surface roughness. Longer pauses allow for more intense discharges, resulting in deeper and more irregular craters. However, excessive *Toff* can negatively affect the machining process by prolonging plasma removal, reducing energy transmission, and further diminishing *MRR*.

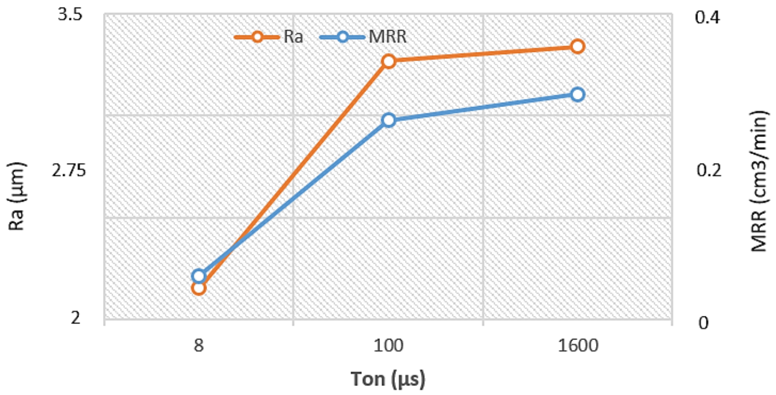

Fig. 2 – Effect of *Ton* on (a) *MRR* and (b) *Ra*.

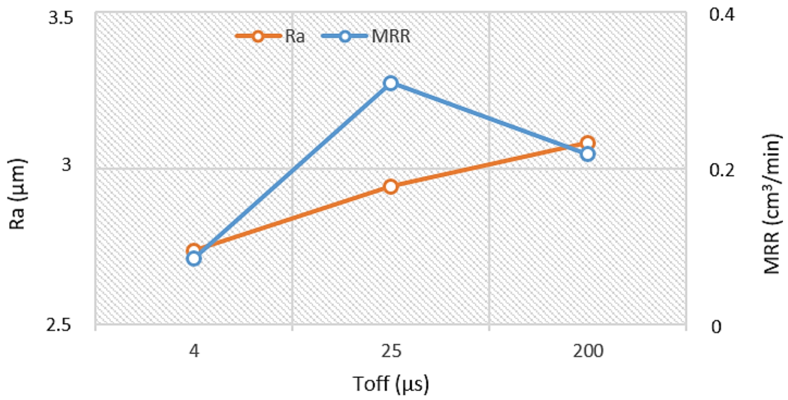

Fig. 3 – Effect of *Toff* on (a) *MRR* and (b) *Ra*.

Optimizing *Toff* is therefore strongly recommended to achieve a balance between *MRR* and *Ra*.

Experimental results have confirmed that current intensity *I* is the most influential parameter affecting both *MRR* and *Ra* in the EDM process. As the current increases, the energy of each discharge grows, leading to larger and deeper craters on the machined surface, which directly affects surface quality. To advance deeper insight into this effect, we focus on analyzing crater dimensions, surface roughness at a microscopic level, and X-ray diffraction (XRD) patterns while varying only the current intensity.

3.2. MEASURED SIZE AND DEPTH OF CRATERS

In order to analyze the influence of the current *I* on surface quality in terms of *Ra*, crater size, and crater depth, *Ton* and *Toff* are fixed at 8 µs and 4 µs, respectively. Microscopic images of the surface roughness as well as the 3d topography of the three examined surfaces (Fig. 4), as measured with the optical profilometer.

Fig. 4 – Examined surfaces according to the selected tests.

The assessment of surface texture quality is conducted in accordance with ASME B46.1-1995 standards, utilizing a comprehensive set of roughness parameters to ensure an accurate and detailed evaluation. The average roughness (*Ra*), which represents the arithmetic mean of profile height deviations from the mean line, provides a general indication of surface smoothness but does not account for extreme peaks and valleys. To complement this, the root mean square roughness (*Rq*) is also measured, offering a more sensitive representation of surface irregularities by giving greater weight to larger deviations. Additionally, the maximum profile peak height (*Rp*) is considered, as it highlights the highest peak within the measured profile. The five-point average maximum height (*Rz*) is used to capture the average height difference between the highest peaks and lowest valleys across multiple sampling lengths, providing a more robust characterization of surface irregularities. The combination of these parameters ensures a comprehensive analysis the surface texture. The different measures are summarized in Table 4.

The required surface roughness of a component depends on the nature of the desired application. In some cases, EDM is therefore utilized as a surface texturing technique rather than merely a material removal process. Consequently, investigating the surface texture is crucial for selecting the appropriate machining parameters. As shown in Fig. 5, the surface quality analysis demonstrates that *Ra* is primarily influenced by the variations in *I*, confirming the evolution curves of Fig. 1.

Table 4

Surface roughness results of machined parts

I (A)	*Ra* (Å)	*Rq* (Å)	*Rp* (Å)	*Rz* (Å)
8	13164.74	18169.76	106645.87	225663.32
24	14144.11	20309.03	159229.87	286692.4
64	28433.84	40998.45	231953	485864.96

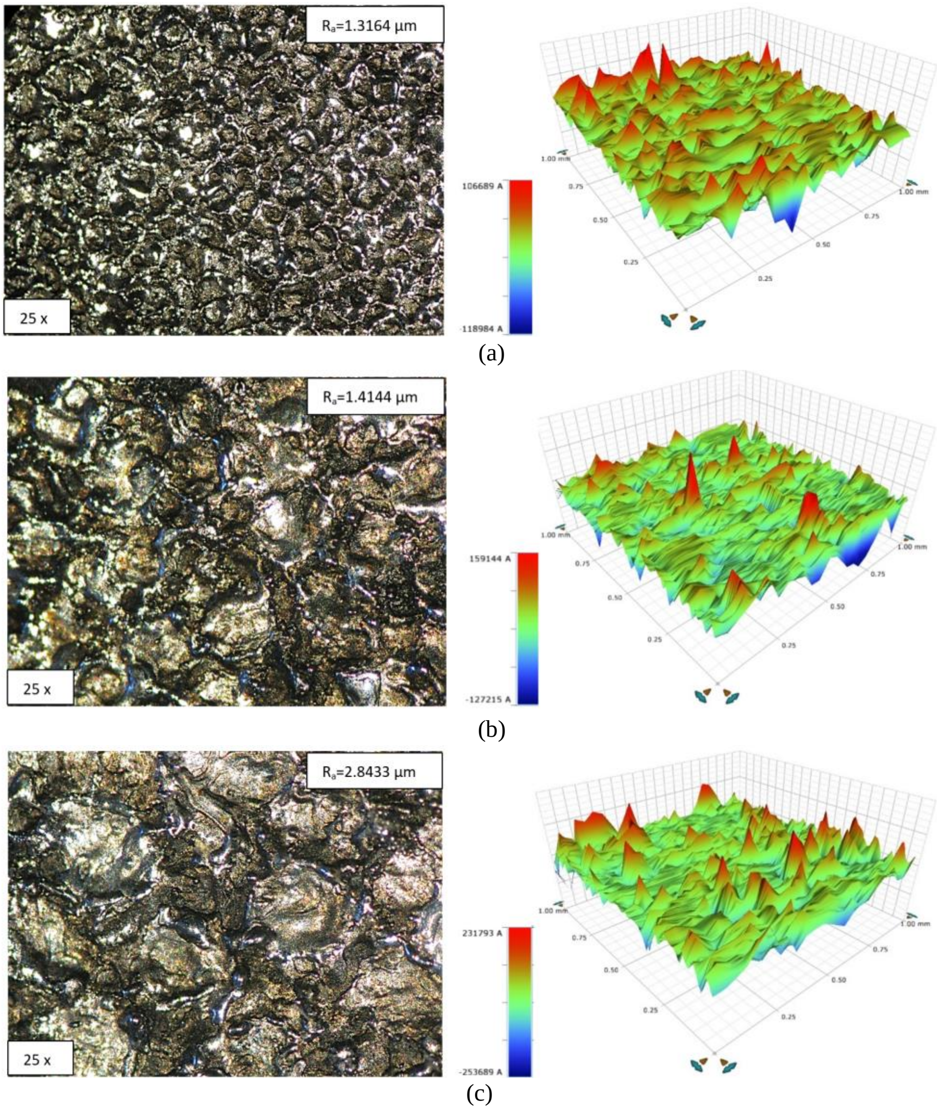

Fig. 5 – Surface roughness microscopic images and 3d surface topography for: a) I = 8 A; b) I = 24 A; c) I = 64 A.

The variation in roughness as a function of *I* results from variations of crater diameter and depth. Crater size is defined as the average diameter (*Dav*) of five craters, while crater depth (*Cd*) is estimated as the maximum profile peak depth. The 50× magnification of the formed craters, along with the evolution of (*Dav*) and Cd as a function of *I*, are presented in Figs. 6 and 7.

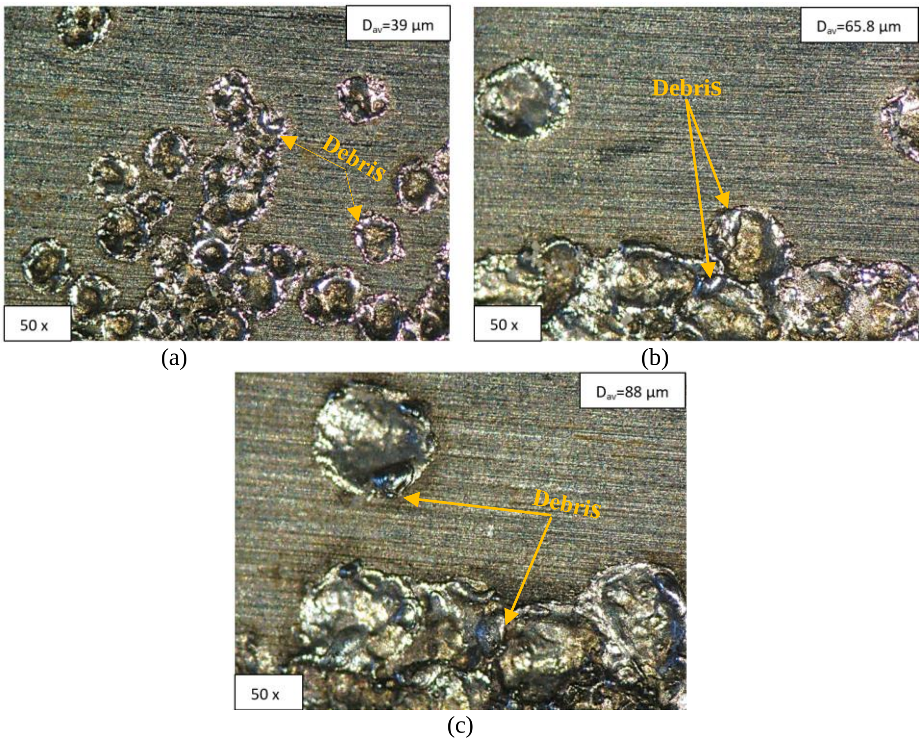

Fig. 6 – EDM craters with: a) I = 8 A; b) I = 24 A; c) I = 64 A; *Dav* = average of five crater diameters.

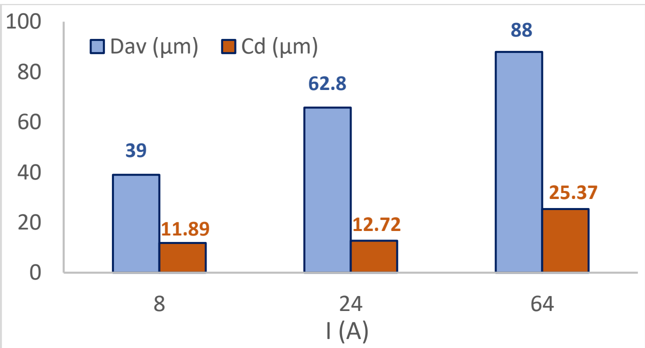

Fig. 7 – *Dav* and *Cd* as function of *I*.

The EDM surfaces with higher *Ra* exhibit larger and deeper craters compared to those with lower *Ra*. As the current *I* increases from 8 A to 64 A, the value of *Dav* more than doubles, rising from 39 µm to 88 µm. The crater diameter proves to be a reliable indicator of the spark action during EDM process. Regarding *Cd*, the change in depth is particularly significant when the current *I* varies from 24 A to 64 A, increasing from 12.72 µm to 25.37 µm. The progressive growth in the size of craters corresponds to the variation in roughness, suggesting that a high EDM current of 64 A produces the roughest surface, in the case of our study.

Debris are also observed on the EDM surfaces. Debris formation occurs when molten material is ejected, falls back onto the surface, and subsequently solidifies taking a spherical shape. In Fig. 6, it is well observed that the size of the formed debris is significantly affected by the increase of *I*. This phenomenon can be attributed to the changes in the material removal mechanism with respect to discharge energy. At lower energy levels, material removal is predominantly governed by vaporization. As discharge energy increases, however, there is a transition from vaporization to melting, leading to an increase in the size of the debris [23].

3.3. MEASURED XRD PATTERNS

The microstructural behavior of machined C45 steel was investigated through XRD analysis as a function of the applied *I*. Diffractograms for both the as received alloy and the machined samples are shown in Fig. 8. The XRD pattern of the base material reveals that the initial structure of C45 is entirely austenitic (A). On the other side, the XRD patterns of the machined C45 samples exhibit an attenuation in the intensity of the main austenitic peaks, accompanied by the emergence of new peaks, which indicates the formation of a cementite phase (C).

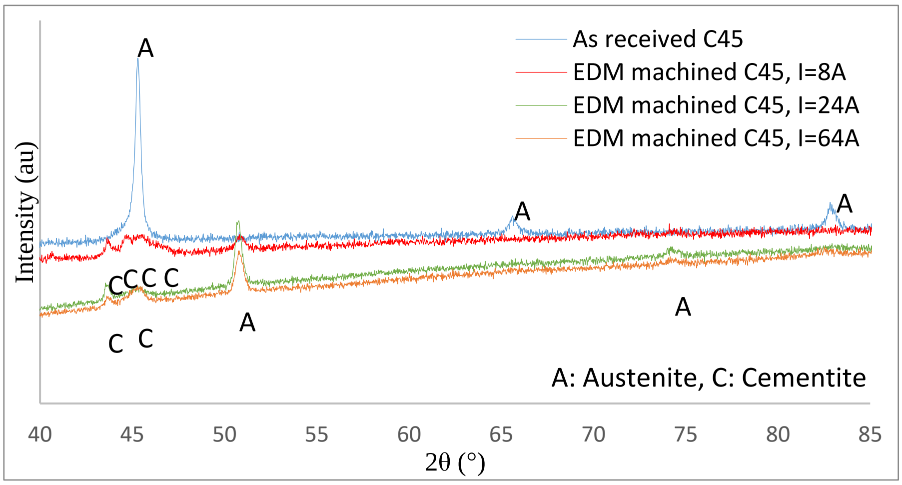

Fig. 8 – XRD patterns of as received and machined C45 for various *I*.

During the EDM process, the temperature of the spark ranges from approximately 10000 to 20000°C [24, 25], leading to material removal from both the tool and workpiece through melting and vaporization. This electrothermal process also results in the formation of a heat-affected zone leading to the formation of new phases, mainly the cementite phase (Fe_3C), due to the phase transformation mechanism [26]. The high carbon content in the machined surface is associated with dielectric cracking, rather than diffusion from the base material [27]. It can also result from the carburization phenomenon. Moreover, it was reported that machining in an oil dielectric promotes the increase of the carbon content [28].

To gain a deeper understanding of the microstructural changes in the examined C45 structure, key parameters such as crystallite size (D) and dislocation density (D_{is}) were calculated from the XRD data using the Debye-Sherrer equations (Equations 2 and 3):

$$D = \frac{K\lambda}{\beta \cos\theta} \tag{2}$$

$$\delta = \frac{1}{{D_a}^2} \tag{3}$$

where λ represents the wavelength of CuK_α radiation (1.5418 Å), β is the full width at half-maximum (in radians) of the diffraction peak, and θ is the diffraction angle at the peak position (in radians). D_a is the average crystallite size.

Cementite is well known as the hardest phase in the iron-carbon alloys, and its presence on EDM machined surfaces contributes to an increase in hardness. This effect is evidenced by a 27% reduction in the average crystallite size D_a as I increases from 8A to 64A. Concurrently, D_{is} increases by approximatively 84%, indicating that higher I leads to a higher dislocation density in the C45 structure (Fig. 9).

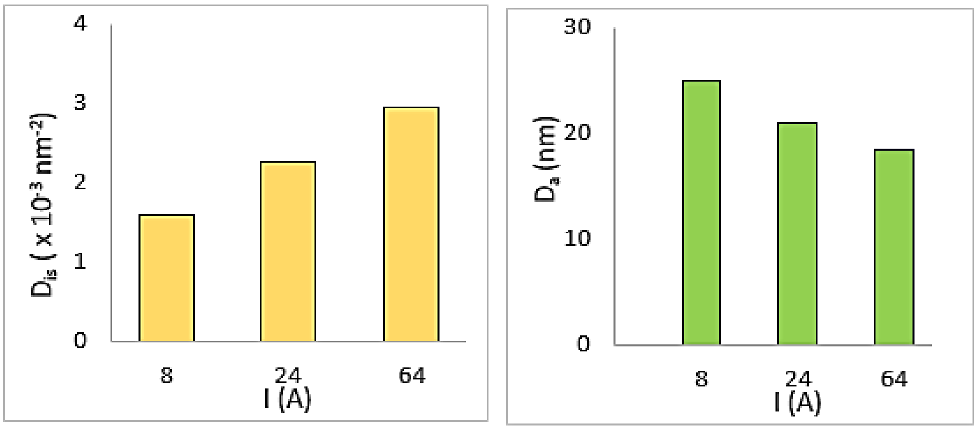

Fig. 9 – D_{is} and D_a of the machined C45 structure as function of I.

This result can be explained by the increase of the residual stress, which results from the combined effects of thermal stress and phase transformation stress [29].

4. CONCLUSIONS

The experimental results demonstrate that *I* is the most influential parameter affecting *MRR* and *Ra* in the EDM process. Higher current levels lead to increased discharge energy, resulting in larger and deeper craters, higher roughness, and greater debris formation. The transition from vaporization-dominated material removal at low *I* to melting-induced erosion at high *I* further amplifies these effects. XRD analysis confirms significant microstructural modifications, including the formation of a cementite phase (Fe_3C), increased dislocation density, and higher residual stresses, which collectively enhance surface hardness.

REFERENCES

1. B. Ben Fraj, T. Kamoun, H. Hentati, M. Trabelsi, N. Ghazouani, and M. Ahmed, *Optimization of forming force and Erichsen index using Taguchi design of experiments: Mathematical models and experimental validation*, Proc. Inst. Mech. Eng. Part B **238**(9), 1316–1326 (2024). https://doi.org/10.1177/09544054231194107.
2. L. F. Folle, T. N. Lima, M. P. S. Santos, B. Callegari, B. C. d. S. Silva, L. G. S. Zamorano, and R. S. Coelho, *A Review on Sheet Metal Forming Behavior in High-Strength Steels and the Use of Numerical Simulations*, Metals **14**, 1428 (2024). https://doi.org/10.3390/met14121428.
3. G. Bokuchava, P. Petrov, G. Genchev, V. Michailov, N. Doynov, et al., *Residual stress analysis in welded joints by neutron diffraction and computer modeling*, Romanian Journal of Physics **63**(7–8), 904 (2018).
4. S. Ammar, B. Ben Fraj, H. Hentati, et al., *Mechanical performances of printed carbon fiber-reinforced PLA and PETG composites*, Proc. Inst. Mech. Eng. Part L J. Mater. Des. Appl. **238**, 1488–1499, (2024). https://doi.org/10.1177/14644207231225761.
5. S. F. Iftekar, A. Aabid, A. Amir, and M. Baig, *Advancements and Limitations in 3D Printing Materials and Technologies: A Critical Review*, Polymers **15**, 2519 (2023). https://doi.org/10.3390/polym15112519.
6. S. Moakhar, H. Hentati, M. Barkallah, J. Louati, M. Haddar, C. Bonk, and B. A. Behrens, *Modeling of the ductile damage – Application for bar shearing*, Mater. Wiss. Werkstofftech. **50**, 1353–1363, (2019). https://doi.org/10.1002/mawe.201800128.
7. S. Pawanr and K. Gupta, *Dry machining techniques for sustainability in metal cutting: a review*, Processes **12**(2), 417 (2024).
8. C. Hammami, N. Kammoun, H. Hentati, et al., *Parametric analysis of the damage characterization tests of aluminum bulk material*, J. Mech. Sci. Technol. **36**, 5019–5025 (2022). https://doi.org/10.1007/s12206-022-0914-z.
9. Y. Kriaa, H. Hentati, and B. Zouari, *Applying the phase-field approach for brittle fracture prediction: Numerical implementation and experimental validation*, Mech. Adv. Mater. Struct. **29**(6), 828–839 (2022). https://doi.org/10.1080/15376494.2020.1795957.
10. A. F. V. Pedroso, V. F. C. Sousa, N. P. V. Sebbe, F. J. G. Silva, R. D. S. G. Campilho, R. C. M. Sales-Contini, and A. M. P. Jesus, *A Comprehensive Review on the Conventional and Non-Conventional Machining and Tool-Wear Mechanisms of INCONEL®*, Metals **13**, 585 (2023).

11. E. Garba, A.M. Abdul-Rani, N.A. Yunus, A.A.A. Aliyu, I.A. Gul, M. Al-Amin, and R. Aliyu, *A Review of Electrode Manufacturing Methods for Electrical Discharge Machining: Current Status and Future Perspectives for Surface Alloying*, Machines **11**, 906 (2023).
12. M. Deja and A.P. Markopoulos, *Advances and Trends in Non-Conventional, Abrasive and Precision Machining 2021*, Machines **12**(2), 138 (2024).
13. J.E.A. Qudeiri, A. Zaiout, A.-H.I. Mourad, M.H. Abidi, and A. Elkaseer, *Principles and Characteristics of Different EDM Processes in Machining Tool and Die Steels*, Appl. Sci. **10**, 2082 (2020). https://doi.org/10.3390/app10062082.
14. Al. Nitu et al., *Characterization of the DHC crack parameters in zirconium alloys*, Romanian Journal of Physics **68**, 910 (2023).
15. M.M. Hasan, T. Saleh, A. Sophian, M.A. Rahman, T. Huang, and M.S. Mohamed Ali, *Experimental modeling techniques in electrical discharge machining (EDM): A review*, Int. J. Adv. Manuf. Technol. **127**(5), 2125–2150 (2023).
16. D. Oniszczuk-Świercz, R. Świercz, A. Kopytowski, and R. Nowicki, *Experimental investigation and optimization of rough EDM of high-thermal-conductivity tool steel with a thin-walled electrode*, Materials **16**(1), 302 (2022).
17. V. Marrocco, F. Modica, V. Bellantone, V. Medri, and I. Fassi, *Pulse-Type Influence on the Micro-EDM Milling Machinability of Si3N4–TiN Workpieces*, Micromachines **11**, 932 (2020). https://doi.org/10.3390/mi11100932.
18. R. Ramachandra, *Optimization of MRR and SR for AISI 316 Stainless steel material by using RSM Technique in EDM machining*, Int. J. Eng. Sci. Math. **6**, 314–321 (2017).
19. D. Doreswamy, D.S. Shreyas, S.K. Bhat, and R. Rao, *Optimization of material removal rate and surface characterization of wire electric discharge machined Ti-6Al-4V alloy by response surface method*, Manufacturing Review **9**(15), 11 (2022).
20. S. Saha and S.K. Choudhury, *Multi-objective optimization of the dry electric discharge machining process*, 2009.
21. S. Singh, S. Maheshwari, and P. C. Pandey, *Some investigations into the electric discharge machining of hardened tool steel using different electrode materials*, J. Mater. Process. Technol. **149**(1–3), 272–277 (2004).
22. V. T. Tran, M. H. Le, M. T. Vo, Q. T. Le, V. H. Hoang, N. T. Tran, et al., *Optimization design for die-sinking EDM process parameters employing effective intelligent method*, Cogent Eng. **10**(2), (2023).
23. M. Tanjilul, A. Ahmed, A. S. Kumar, and M. Rahman, *A study on EDM debris particle size and flushing mechanism for efficient debris removal in EDM-drilling of Inconel 718*, J. Mater. Process. Technol. **255**, 263–274 (2010), https://doi.org/10.1016/j.jmatprotec.2017.12.016.
24. P. K. Patowari, U. K. Mishra, P. Saha, and P. K. Mishra, *Surface modification of C40 steel using WC-Cu P/M green compact electrodes in EDM*, Int. J. Manuf. Technol. Manag. **21**, 83–98 (2010). https://doi.org/10.1504/IJMTM.2010.034288.
25. P. K. Patowari, P. Saha, and P. K. Mishra, *Taguchi analysis of surface modification technique using W-Cu powder metallurgy sintered tools in EDM and characterization of the deposited layer*, Int. J. Adv. Manuf. Technol. **54**, 593–604 (2011). https://doi.org/10.1007/s00170-010-2966-y.
26. A. S. Gill and S. Kumar, *Investigation of micro-hardness in electrical discharge alloying of En31 tool steel with Cu–W powder metallurgy electrode*, Arab. J. Sci. Eng. **43**, 1499–1510 (2018).
27. G. Cusanelli, A. Hessler-Wyser, F. Bobard, R. Demellayer, R. Perez, and R. Flükiger, *Microstructure at submicron scale of the white layer produced by EDM technique*, J. Mater. Process. Technol. **149**(1–3), 289–295 (2004). https://doi.org/10.1016/j.jmatprotec.2003.11.047.
28. J. Murray, J. C. Walker, and A. T. Clare, *Nanostructures in austenitic steel after EDM and pulsed electron beam irradiation*, Surface and Coatings Technology **259**, 465–472 (2014).
29. G. Wang and F. Han, *Influence of superimposed pulse position in superimposed pulse current waveform on surface integrity in electrical discharge machining*, Int. J. Adv. Manuf. Technol. **132**, 3179–3191 (2024). https://doi.org/10.1007/s00170-024-13454-6.